JOURNAL OF GEOPHYSICAL RESEARCH, VOL. 91, NO. B8, PAGES 8314-8324, JULY 10, 1986

STRETCHING INSTABILITIES AND LITHOSPHERIC BOUDINAGE

Yanick Ricard and Claude Froidevaux

Laboratoire de Géodynamique, Université de Paris-Sud, Orsay, France

Abstract. A competent layer with a nonlinear rheology can, under extension, exhibit pinch-and-swell instabilities. Such instabilities can explain small-scale regular deformations of rock. Recently they have also been invoked in relation to the distribution of basins and ranges (Fletcher and Hallet, 1983) and the undulation of the Bouguer map (Froidevaux, 1986) in the western part of North America. For the case of a simple stratified structure, different authors have expressed mathematical solutions describing these instabilities. In this paper we elucidate the general physical meaning of these nonhomogeneous deformations. In the simplest case where the competent layer is fully embedded in a softer material, a fundamental mode develops with a preferred wavelength equal to 4 times the thickness of a competent layer. The novelty is the occurrence of overtones with alternate symmetrical and antisymmetrical deflections of the interfaces between layers. These modes have a large amplitude when the rheology tends to perfect plasticity. The presence of a free surface like the earth's surface for the upper crust is shown to double the preferred wavelength of the fundamental mode and to forbid one overtone out of two. This new effect is caused by gravity which inhibits the growth of surface topography. Another shift is of opposite sign to that caused by a free surface. Numerical solutions for multilayer structures can elucidate the nature of couplings between various layers. The case of a three-layer lithosphere having a soft lower crust and overlying a mantle asthenosphere has been analyzed in some detail. It shows that, in the range of wavelengths larger than 30 km, up to five preferred modes may be superimposed. This should encourage further analysis of the western U.S. topography and gravity pattern which is known to contain at least two wavelengths: about 40 km for the individual basins and ranges and about 200 km for the Bouguer troughs in Nevada and their associated broad topographies.

Introduction

Boudin is the French name for blood sausage, called black pudding by the British. The name has been used by geologists to describe deformed rock layers with pinches and swells. It has quickly been realized that these structures had been formed as strong layers embedded in a weak matrix were elongated. Such small-scale observations have suggested that the distance betwen successive pinches amounts to a small multiple of the layer thickness. The basic physical problem consists therefore in unraveling the mechanisms of these stretching instabilities, and in predicting their growth rate and preferred wavelengths. Large-scale deformation like the rather regular succession of basins and ranges in western North America has also been looked at in terms of a grand crustal boudinage (Fletcher and Hallet, 1983). Here, the wavelength is 40 km. Similar regularities in the distribution of rifts are found in the recent extensional deformation of Tibet and possibly in the Early Tertiary phase of tectonics in northeastern China (Armijo et al., 1982; Ma et al., 1984; Froidevaux and Ricard, 1985). For a still larger depth range, boudinage instabilities have been invoked for the mantle lithosphere in order to account for a striking 200 km wavelength undulation of the Bouguer map in the Basin and Range province of North America (Froidevaux, 1986).

The concept of crustal or lithospheric boudinage requires knowledge of the deformation pattern at depth. For examples, the Moho and lithosphere-asthenosphere boundary configurations ought to be compared with surface observables like topography and gravity. This information about deep structures is not usually available, although recent results of reflection seismology by the Consortium for Continental Reflection Profiling (COCORP) have shed some light on the Moho geometry in the Basin and Range. Regional seismic tomography (Humphreys et al., 1984; Marillier and Mueller, 1982; Montagner, 1986) will certainly be needed to constrain the problem.

In the present paper, the physics of instabilities induced by extensional or compressional tectonics will be presented. Any attempt at predicting the exact structures of a specific geological case seems to be difficult before the geophysical data set is improved. First, we shall define the physical laws and appropriate boundary conditions. Our approach is based on the study of marginal instabilities for layers of finite thickness. It is akin to earlier formulations (Johnson, 1977). A particular effort has been made to derive simple analytical solutions for the induced transverse perturbations caused by the main deformation. Specific selection rules for the preferred wavelengths of boudinage or folding are given, and their physical meaning is elucidated. The analysis is then extended to investigate the action of gravity which tends to hamper the surface topography. Furthermore, the geodynamically important influence of a narrow intracrustal or sublithospheric soft channel has been quantitatively tested. The physical insight gained is related to the occurrence of fundamental modes and overtones for the instability. It helps to understand the final solutions for stratified lithospheric structures with various thicknesses, densities, and viscosities.

Physical Model

Let us consider a stratified structure made up of parallel layers of varying thickness and mechanical properties. When such a structure is stretched, or compressed, each layer will become

Paper number 5B5795.
0148-0227/86/005B-5795$05.00

thinner, or thicker. However, the deformation can be inhomogeneous; it is made up of a large-scale basic flow and smaller-scale instabilities. The basic problem of the buckling of a compressed, competent layer surrounded by a viscous fluid has been treated in the thin plate approximation (Biot, 1961; Ramberg, 1963). It shows the existence of selected wavelengths for the folds. More general studies with layers of finite thicknesses and nonlinear rheologies have shown that the mathematical treatments are identical for stretching and compression (Smith, 1977, 1979). In particular, the characteristic wavelengths of boudinage and folding are predicted to be equal. Comparisons between theory and laboratory experiments have been satisfactory (Biot et al., 1961; Ramberg, 1955; Neurath and Smith, 1982). For tectonic structures involving the whole crust or lithosphere, the above physical approach is applicable (Fletcher and Hallet, 1983; Zuber et al., 1986). It requires the choice of realistic rheologies, a nontrivial proposal.

Basic Equation

The model lithosphere consists of horizontal layers, each having a uniform density ρ and viscosity η. A power law (Johnson, 1977) between creep rate $\dot{\epsilon}$ and stress σ is assumed. It implies an effective viscosity of the form

$$\eta=A((\sigma_{xx}-\sigma_{zz})^2+4\sigma_{xz}^2)^{\frac{1-n}{2}} \quad (1)$$

Here A is a proportionality factor, n the power law coefficient, and x and z the horizontal and vertical axes.

Starting from the constitutive equations one can derive the following relationships (Smith, 1977, 1979; Fletcher, 1974):

$$\begin{aligned}\tilde{\sigma}_{xx}&=2\frac{\bar{\eta}}{n}\tilde{\dot{\epsilon}}_{xx}-\tilde{p}\\ \tilde{\sigma}_{zz}&=2\frac{\bar{\eta}}{n}\tilde{\dot{\epsilon}}_{zz}-\tilde{p}\\ \tilde{\sigma}_{xz}&=2\bar{\eta}\tilde{\dot{\epsilon}}_{xz}\end{aligned} \quad (2)$$

Here $\tilde{\dot{\epsilon}}$, $\tilde{\sigma}$, and the pressure $\tilde{p}$ define the perturbations with respect to a time independent basic flow $\bar{\dot{\epsilon}}$. The viscosity $\bar{\eta}$ refers to that seen by the basic flow. One notices in (2) that extensional or compressional perturbations are easier along the principal axes of the basic flow x and z.

Equations (2) can be combined with mass and momentum conservation relationships. The solving procedure consists of trying out sinusoidal dependences along the horizontal axis x with wavelength λ (Fletcher and Hallet, 1983; Ricard, 1986). It yields general solutions for the stresses and the vertical and horizontal velocities $\tilde{w}$, $\tilde{u}$ as a linear combination of four terms (see Appendix A). The four coefficients of the general solutions must be determined on the basis of the boundary conditions at each interface.

Boundary Conditions

The planar geometry of a given interface is assumed to be perturbed by a sinusoidal undulation of amplitude h(t)cos(kx). The growth of this perturbation at the time t is $\dot{h}(t)\cos(kx)$, and its magnitude is equal to the vertical velocity $\tilde{w}+\bar{\dot{\epsilon}}_{xx}h$ at this interface. The velocities and stresses are continuous across a perturbed interface. From this statement one derives the following linearized expressions for the perturbing components of the stresses (Johnson, 1977):

$$\begin{aligned}\tilde{\sigma}^a_{zz}-\tilde{\sigma}^b_{zz}&=(\rho_a-\rho_b)gh\cos kx\\ \tilde{\sigma}^a_{xz}-\tilde{\sigma}^b_{xz}&=4(\bar{\eta}_a-\bar{\eta}_b)\bar{\dot{\epsilon}}_{xx}kh\sin kx\end{aligned} \quad (3)$$

The indices a and b refer to the media above and below the interface. The right-hand side of the first relationship expresses the buoyancy of the deflected boundary. In the second relationship, the right-hand side is proportional to the difference in deviatoric stresses related to the basic flow on both sides of the deflected boundary. The deformation of an interface is therefore driven by this combination of gravity and rheological effects. These two conditions and the continuity of the vertical and horizontal velocities represent the required boundary conditions.

The Growth Rate Factor q

Our numerical solving algorithm (Ricard, 1986) is somewhat simpler than what other authors have done. The deformations h_i of the m interfaces are proportional to a linear combination of the growth rates $\dot{h}_1$ to $\dot{h}_m$. The problem is solved by computing the eigenvalues and the eigenvectors of this transformation. These eigenvalues can be defined as $q_i\bar{\dot{\epsilon}}_{xx}$. The solutions can therefore be expressed as linear combinations of the eigenvectors, each one multiplied by the corresponding time dependent factor $\exp(q_i\bar{\dot{\epsilon}}_{xx}t)$. The largest eigenvalue, which we shall label q, dominates the evolution of all interfaces. This marginal stability analysis only predicts initial growth rates. Final deformations are inaccessible to it. As an illustration, with a stretching amplitude $\bar{\dot{\epsilon}}_{xx}t$ of 50%, a growth rate factor of 9 enhances the initial perturbation by a factor $\exp(9/2)=90$. This shows how to use the computed values of q presented in the remaining sections of this paper.

Deformation of a Strong Layer Embedded in an Infinite Medium

The basic approach presented in the above section will enable us to treat some cases with simple geometry in order to gain physical insight. A simplified formulation of the problem will also be given and used to find analytical solutions in this section and the next one.

Wavelength Selection

The simplest geometry to consider consists of a layer of thickness H_1 between two identical half-spaces. The whole structure is either stretched or compressed horizontally. The occurrence of boudinage instabilities is known to require power law rheologies with large n values. Once this exponent exceeds 100, an asymptotic behavior is reached which is identical to perfect plasticity (Fletcher and Hallet, 1983). Here one takes $n_1=1000$ for the strong layer and $n_2=3$ for the half-spaces. The central layer is 100 times more viscous than its surroundings. All layers have identical density. The value n=3 is close to

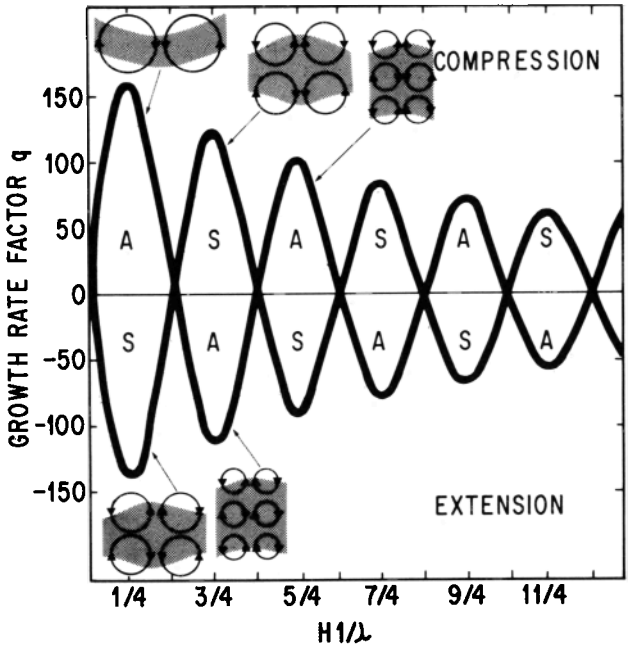

Fig. 1. Growth rate factor q versus inverse wavelength for the instability of a competent layer of thickness H_1 imbedded in an infinite matrix of low strength. The horizontal wavelength λ is expressed in a nondimensional form in terms of H_1. The competent layer has a highly nonlinear rheology (n=1000), and the surrounding matrix has a rheology with n=3. All layers have the same density so that gravity has no influence on the growth of instabilities. These solutions were computed numerically. The upper curve corresponds to instabilities caused by compression parallel to the plane of the competent layer, whereas the lower curve applies to extension. The schematic velocity patterns of the first modes of deformation are depicted by small cartoons. The letters S and A refer to the symmetry or antisymmetry of this velocity pattern with respect to the central plane of the layer of thickness H_1.

what comes out of laboratory experiments for high-temperature creep of minerals. However, the presence of faults in the seismic crust or of ductile shear zones in the hotter portion of the lithosphere is expected, on a macroscopic scale, to correspond to a more complicated rheology. The choice of a large value for n_1 is an attempt to come closer to the actual lithospheric rheology.

Following the procedure described in the previous section, the maximum eigenvalue was computed both for stretching and compression. The corresponding growth rate factor q versus H_1/λ is plotted in Figure 1. The upper curve corresponds to a compressional basic flow ($\dot{\bar{\epsilon}}_{xx}>0$), whereas the lower curve applies to extensional flow ($\dot{\bar{\epsilon}}_{xx}<0$). The growth rate $q\dot{\bar{\epsilon}}_{xx}$ is always positive except for discrete values of the wavelength $\lambda = 4H_1/2j$ where j is an integer. The fundamental mode of the deformation instability is found for $\lambda \simeq 4H_1$, but overtones at $\lambda \simeq 4H_1/3$, $4H_1/5$,... are also present.

The fundamental mode corresponds to buckling in compression and boudinage in extension, as shown by the cartoons inserted next to each curve. One notices that in compression the fundamental velocity mode is represented by a single cell flowing through the central layer as its boundaries deflect. Similarly, two open cells characterize the fundamental mode for extension. The velocity field of the shorter-wavelength modes includes additional cells, as indicated by the other cartoons. One notices that for a given basic flow, either compressional or extensional, the instability is alternatively symmetrical (type S in Figure 1) or antisymmetrical (type A). In other words, both boudinage and buckling can simultaneously be present.

The vertical velocity maximum is not always located at the interfaces. The deformation inside the competent layer can be stronger than on its boundaries. However, when the growth rate at the interfaces becomes zero, the perturbing flow vanishes everywhere inside the layer.

The preferred values of λ are the same for compressional and extensional instabilities. The corresponding selection rules can be written in the following way: $2H_1 = j\lambda + \lambda/2$. In wave propagation, an analogous condition applies for constructive interferences between an incident and reflected wave at a distance H_1 from a mirror. In our problem, a sinusoidal undulation of horizontal wavelength λ at one interface induces vertical velocities in layer 1 during stretching or compression. Vertically, according to (A1) and (A2), the velocity has a wavelength $\lambda_1 = \lambda/\beta_1 = \lambda\sqrt{n_1/(n_1-1)}$. For large n values, both horizontal and vertical wavelengths are about equal.

Amplitude of the Overtones

The decrease of the overtone amplitudes for large wave numbers is related to the exponential decrease with depth of the physical quantities $\tilde{u}$, $\tilde{w}$, $\tilde{\sigma}_{xz}$, $\tilde{\sigma}_{zz}$. This depth dependence is expressed by equation (A1). It shows that the decay of the perturbing flow depends on $\exp(-2\pi H_1/\lambda\sqrt{n_1})$. The larger the power law exponent n, the larger the number of overtones with high amplitudes. When the viscosity is more linear ($n_1 \rightarrow 1$), the envelope of the growth rate maxima decreases more sharply than in Figure 1. At the same time, the amplitude of the fundamental mode vanishes. For a discontinuous strength stratification, the use of large n values leads to the existence of high-amplitude overtones. A continuous viscosity distribution would lead to a steeper falloff of the higher order peaks in the q versus H_1/λ diagram (Fletcher and Hallet, 1983). The viscosity variation over a depth range comparable with the horizontal wavelength λ decreases with λ in the case of a continuous strength stratification. Therefore the growth rate of the deformation, proportional to the viscosity variations, diminishes sharply with λ. However, these overtones still exist for a continuous viscosity distribution with a large power law exponent (Zuber et al., 1986). In a following section we shall see that for the real earth the effect of surface gravity tends to damp the fundamental mode. This effect increases by comparison the importance of the higher-order modes of deformation.

Analytical Formula for the Growth Rate of an Instability

The growth rate factor which was computed numerically for Figure 1 can also be obtained

analytically if one makes the assumption that the tranverse deformation of the strong layer has to be either symmetrical (boudinage) or antisymmetrical (folding). We find

$$q=\pm 2n_1\left(1-\frac{\bar{\eta}_2}{\bar{\eta}_1}\right)(Q^2-1\pm\frac{\beta_1}{\alpha_1}\frac{1}{\sin(\beta_1 kH_1)}((Q^2+1)\sin(\beta_1 kH_1)+2Q\cos(\beta_1 kH_1)))^{-1} \quad (4)$$

where

$$Q=\frac{\bar{\eta}_2}{\bar{\eta}_1}\sqrt{\frac{n_1}{n_2}} \qquad \alpha_1=\sqrt{\frac{1}{n_1}} \qquad \beta_1=\sqrt{\frac{n_1-1}{n_1}}$$

One verifies that q vanishes when the sin function is zero, i.e., when $\lambda=2\beta_1 H_1/j$. The plus and minus signs respectively correspond to buckling and boudinage. An equivalent expression has been derived earlier, for the case of buckling only (Fletcher, 1974). The agreement between (4) and the computed values of Figure 1 is perfect.

A simplified analysis will now be presented for boudinage. It is somewhat akin to the thin plate approximation applicable only to buckling (Biot, 1961). Our mechanical reasoning will be restricted to long wavelengths and will include the effect of gravity. We consider the same structure as above, a single layer between two half-spaces, but also include a density difference $\delta\rho$. The central layer has thus a density ρ, and the lower and upper half-spaces have densities $\rho+\delta\rho$ and $\rho-\delta\rho$. When the deformations are symmetrical, the gravity forces at the interface are also symmetrical. If $\delta\rho$ is taken as positive, the gravitational forces will be stabilizing. They will be destabilizing for negative $\delta\rho$ values. We shall assume the deformation is symmetrical under stretching.

Expressing the stress deviator and averaging vertically over the depth range of the central layer ($-H_1/2<z<H_1/2$) one finds

$$\langle\tilde{\sigma}_{zz}\rangle-\langle\tilde{\sigma}_{xx}\rangle=4\frac{\bar{\eta}_1}{n_1}\frac{1}{H_1}\int\dot{\tilde{\epsilon}}_{zz}dz=8\frac{\bar{\eta}_1}{n_1}\frac{\dot{h}}{H_1} \quad (5)$$

From the equilibrium equation one can derive $\langle\tilde{\sigma}_{xx}\rangle$:

$$-k\langle\tilde{\sigma}_{xx}\rangle+2\frac{\tilde{\sigma}^b_{xz}}{H_1}=0 \quad (6)$$

Here $\tilde{\sigma}^b_{xz}$ is the shear stress at the top interface within the layer. Similarly, one can define $\tilde{\sigma}^b_{zz}$. The shear stress is antisymmetrical with respect to the middle of the system. If z is measured vertically from the middle of the competent layer, it amounts to $\tilde{\sigma}_{xz}=2\tilde{\sigma}^b_{xz}\,z/H_1$ to first order. An integration by parts yields $\langle\tilde{\sigma}_{zz}\rangle$:

$$\langle\tilde{\sigma}_{zz}\rangle=\frac{1}{H_1}\int\tilde{\sigma}_{zz}dz=\tilde{\sigma}^b_{zz}-\frac{1}{H_1}\int\frac{\partial\tilde{\sigma}_{zz}}{\partial z}z\,dz=\tilde{\sigma}^b_{zz}+\frac{k}{H_1}\int\tilde{\sigma}_{xz}z\,dz$$

$$\langle\tilde{\sigma}_{zz}\rangle=\tilde{\sigma}^b_{zz}+\frac{1}{6}kH_1\tilde{\sigma}^b_{xz} \quad (7)$$

Here the vertical derivative of $\tilde{\sigma}_{zz}$ was expressed in terms of $\tilde{\sigma}_{xz}$ according to the equilibrium equation. Substituting (6) and (7) into (5) one obtains a relationship between the growth rate h and the boundary stresses inside the layer.

$$8\frac{\bar{\eta}_1}{n_1}\frac{\dot{h}}{H_1}=\tilde{\sigma}^b_{zz}-\frac{2}{kH_1}\tilde{\sigma}^b_{xz}\left(1-\frac{1}{12}k^2H_1^2\right) \quad (8)$$

Equations (3) relate the stresses $\tilde{\sigma}^b$ below one interface to the stresses $\tilde{\sigma}^a$ above it. In Appendix B we show that $\tilde{\sigma}^a$ can be expressed in terms of the boundary deflection h and its growth rate $\dot{h}$. The calculation is carried out to the same order of approximation as in (7). It yields

$$\tilde{\sigma}^b_{zz}=\delta\rho gh-2\frac{\bar{\eta}_2}{\sqrt{n_2}}k(\dot{h}-\dot{\bar{\epsilon}}_{xx}h)$$

$$\tilde{\sigma}^b_{xz}=4(\bar{\eta}_1-\bar{\eta}_2)\dot{\bar{\epsilon}}_{xx}kh+\frac{\bar{\eta}_2}{\sqrt{n_2}}\frac{1}{H_1}(\dot{h}-\dot{\bar{\epsilon}}_{xx}h)\left(1-\frac{1}{12}k^2H_1^2\right) \quad (9)$$

By combination with (8) this leads to an expression of the growth rate factor q, $q=\dot{h}/\dot{\bar{\epsilon}}_{xx}h$ for long-wavelength boudinage,

$$q=1-n_1\left(1-\frac{\bar{\eta}_2}{\bar{\eta}_1}\right)\frac{1-\frac{1}{12}k^2H_1^2-\frac{\delta\rho gH_1}{8\bar{\eta}_1\dot{\bar{\epsilon}}_{xx}}}{1+\frac{\bar{\eta}_2}{\bar{\eta}_1}\frac{n_1}{\sqrt{n_2}}\frac{1}{kH}\left(1+\frac{1}{12}k^2H_1^2\right)} \quad (10)$$

In the next section, we shall treat some cases showing the agreement of this approximation with numerical solutions. The agreement is better than that obtained for buckling under compression for the well-known thin plate approximation (Biot, 1961; Fletcher, 1974). Using our symbols the latter relationship reads

$$q=n_1\frac{1+\frac{\delta\rho gH_1}{2\bar{\eta}\dot{\bar{\epsilon}}_{xx}}\frac{1}{k^2H_1^2}}{\frac{1}{12}k^2H_1^2+\frac{\bar{\eta}_2}{\bar{\eta}_1}\frac{n_1}{\sqrt{n_2}}\frac{1}{kH_1}} \quad (11)$$

In all expressions (4), (10), and (11) one encounters the characteristic physical parameter $(\bar{\eta}_2/\bar{\eta}_1)\sqrt{n_1/n_2}$. Both approximations (10) and (11) are equivalent at large wavelengths and yield negative growth rates at short wavelengths. In particular, q vanishes for k=0. Notice that for boudinage the growth rate has a maximum value equal to n_1, whereas q may diverge in the case of buckling (Smith, 1979). The driving or retarding effect of gravity forces, expressed by the terms containing $\delta\rho$, is quite different for boudinage and buckling. In the boudinage the variation of q with wavelength is not changed very much by the gravity term. However, when $\delta\rho gH_1=8\bar{\eta}_1\dot{\bar{\epsilon}}_{xx}$, one may see by inspection of (8) and (9) that to first order $\langle\tilde{\sigma}_{xx}\rangle-\langle\tilde{\sigma}_{zz}\rangle=0$. The vanishing stress deviator leads to a vanishing growth rate of the instabilities. For $\delta\rho gH_1>8\bar{\eta}_1\dot{\bar{\epsilon}}_{xx}$, the growth rate becomes negative, i.e., the stabilizing action of gravity dominates. In the case of buckling, the gravity term contains the wavelength. For large wavelengths (k=0), the growth rate will become negative or strongly positive depending upon the sign of $\delta\rho$. The gravitational component of the induced instabilities is much more important for compression. For a stabilizing density contrast, a well-known illustration is the fact that whole crust pinches and swells are easier to form than whole crustal folds.

Asymmetrical Solutions

The application of the physical concepts explained in the above section to the case of the earth's crust or lithosphere requires the consideration of asymmetrical structures. First, we shall analyze the consequences of the existence of a free upper boundary. Second, we shall study the effect of a narrow asthenospheric channel.

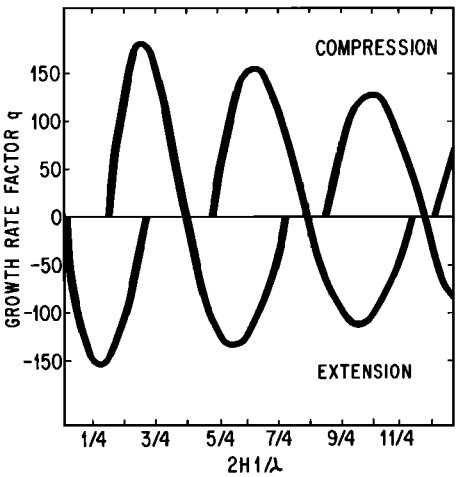

Fig. 2. Computed growth rate factor q versus $2H_1/\lambda$ for a competent layer of thickness H_1 with a free surface at the top and underlain by a weaker infinite half-space. Other characteristics are identical with those corresponding to Figure 1. Gravity causes the occurrence of alternating forbidden bands. It also doubles the values of the preferred wavelengths defined by the maxima of q .

Wavelength Doubling Imposed by a Free Surface

Let us consider a layer of thickness H_1 and power law n_1 overlying a half-space with power law exponent n_2. The viscosity and density are again $\bar{\eta}_1$, ρ_1, and $\bar{\eta}_2, \rho_2$. Depending upon the chosen sign of $\delta\rho = \rho_2 - \rho_1$, one can investigate the instabilities at the crust-mantle or lithosphere-asthenosphere boundary. The induced surface relief will be the result of two competing factors: gravity will tend to damp the topography, whereas stretching or compressional instabilities will tend to enhance this topography. If the global deformation is driven by large deviatoric stresses, a given surface deflection will be of negligible weight. In that case, the effect of gravity can be ignored. The deformation can again be either symmetrical or antisymmetrical, and the instability flow pattern and preferred wavelength conditions should be close to those discussed in the previous section. On the other hand, gravitational forces can dominate the local dynamic behavior if the global deviatoric stresses are weak. In such a situation, the free surface will tend to remain fairly flat, and the deformation of the competent crustal layer will be asymmetrical.

A qualitative understanding of this last case can be derived from the assumption that the vertical velocity vanishes at the free surface. In other words, its variation within the layer exhibits a nodal point at the surface. The same is true for shear stress. Such a pattern of deformation was previously found to prevail in the middle of a layer undergoing boudinage instability (type S in Figure 1). One can thus define an equivalent layer thickness $2H_1$, so that the q maxima now correspond to the selection rule $\lambda = 8H_1/(2j+1)$. Half of the modes (type A) seen in Figure 1 are now incompatible with the condition of a vanishing velocity at the free surface, i.e., in the middle of the equivalent layer. Alternating forbidden bands now exist for the compressional and extensional regimes. In particular the fundamental mode in compression now has a wavelength 3 times shorter than the fundamental mode in extension.

These simple arguments showing how the presence of a free surface forbids certain modes and shifts the preferred wavelength values can be compared with numerical solutions. Figure 2 depicts the growth rate factor q for the structure made up of a strong layer over a half-space. Its upper surface is free and allowed to deform. For simplicity the only density contrast is at the surface, so that $\rho_1 = \rho_2$. The top surface is slightly deformed, and its concavity is either the same as or the opposite of that of the lower interface. The forbidden bands are not as broad as in the extreme case where the top surface deflection is required to vanish completely. At long wavelengths, one comes close to this extreme situation. For higher harmonics, internal stresses allow the development of larger relief, and the forbidden bands get narrow.

Figure 3 depicts a set of q curves for the fundamental mode of boudinage. Curve e was obtained analytically from (11) for an equivalent layer of thickness $2H_1$. The curves a to d were

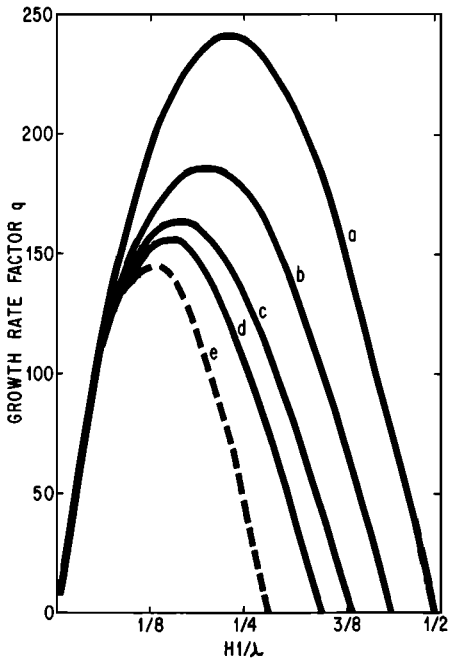

Fig. 3. Growth rate factor q versus nondimensional inverse wavelength for the fundamental mode of boudinage. Each curve corresponds to a given intensity of the gravitational stresses compared to the extensional stresses. This last parameter is expressed by the value of the ratio $\rho_1 g H_1 / 4\bar{\eta}_1 \dot{\bar{\epsilon}}_{xx}$, which increases and amounts to 0, 1, 2, and 3 for the solutions labeled a, b, c, and d. The dashed curve, marked e, corresponds to the analytical solution derived from equation (19) for an equivalent layer of thickness $2H_1$. This double layer should be identical to a case where the above ratio is infinite, i.e., where the surface is completely hampered, as explained in the text.

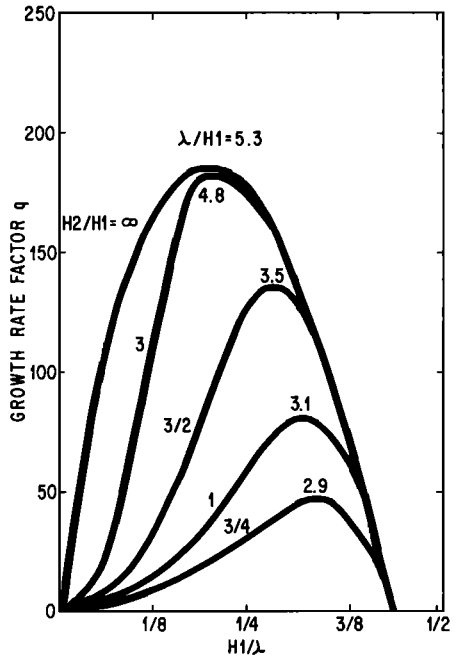

Fig. 4. Growth rate factor q for the fundamental mode of boudinage of a competent layer of thickness H_1 overlying a soft channel of varying thickness H_2. Other characteristics are unchanged in comparison with previous figures. As the weak channel becomes narrower, i.e., as the labeled parameter H_2/H_1 decreases, the maximum of the curve shifts to a smaller wavelength value. This preferred wavelength λ/H_1 is also indicated next to each solution.

numerically computed for various values of the stretching deviatoric stresses. This set of curves illustrates the physical validity of the approximation derived with an equivalent layer of double thickness. These results also illustrate how actual boudinage instabilities can have a dominant wavelength between 4 and 8 times the thickness of the strong layer.

Wavelength Reduction Related to a Soft Channel

The rheological behavior of the lithosphere can be approached by considering a stratified viscosity structure. The deformation of the upper crust occurs by brittle failure. This seismic layer is considered to be mechanically stronger than the warmer ductile lower crust. Below the Moho, the mantle lithosphere is relatively strong because olivine is less ductile than crustal minerals. At greater depths, the temperature dependence may eventually be balanced by a pressure dependence which has not yet been fully documented by laboratory experiments. The width of the asthenospheric channel is thus essentially derived from geodynamical arguments (Fleitout and Yuen, 1984). Here, we shall consider a simple structure consisting of a strong top layer overlying a soft channel. As before, the layers are characterized by a thickness H_1 or H_2, a viscosity $\bar{\eta}_1$ or $\bar{\eta}_2$, a power law coefficient n_1 or n_2, and a density ρ_1 or ρ_2. The boundary conditions at the base of the soft channel are chosen to be no slip for the perturbation flow. A set of solutions have been computed. They correspond to various values of the width H_2 of the asthenospheric channel. The growth rate factor q of the fundamental boudinage mode is plotted in Figure 4. The line for an infinite channel width is taken from Figure 3 (curve b). The other lines depict new solutions and are labeled according to the value of H_2/H_1. For all cases the same stretching deviatoric stress is applied; other parameters are specified in the figure caption. As the channel becomes narrower, the growth rate decreases and its maximum is shifted to shorter wavelength. The value of λ/H_1 at the maximum is also given for each curve. One sees that the dominant wavelength is reduced by a factor of about 2 when one compares the solution for an infinite asthenosphere to the solution where the channel is of equal thickness with the strong layer.

Boudinage of a Three-Layer Lithosphere

In the last two sections, it was shown that a layer with a strongly nonlinear rheology develops stretching instabilities. When gravity effects are negligible, the fundamental mode is centered around a wavelength equal to 4 times the thickness of the competent layer: $\lambda = 4H$. The overtones, with wavelengths 3, 5, 7,... times shorter than the fundamental, represent alternatively buckling and boudinage modes. The action of gravity at the surface tends to hamper the buildup of high topographies. This effect forbids certain instability modes and tends to double the wavelength of the fundamental mode. On the other hand, the presence of a low-viscosity channel shifts the preferred wavelength to smaller values. The mechanical response of stratified structures like the earth's lithosphere can in principle be analyzed in those terms. Several idealized lithospheric models were submitted to stretching, and the growth rate and configuration of instabilities analyzed.

The model lithosphere now consists of a strong upper crust with H_1, $\bar{\eta}_1$, n_1, ρ_1, a soft lower crust with H_2, $\bar{\eta}_2$, n_2, ρ_2, and a strong mantle lithosphere with H_3, $\bar{\eta}_3$, n_3, ρ_3. This three-layer lithosphere is underlain by a half-space asthenosphere with $\bar{\eta}_4$, n_4, ρ_4. Table 1 shows that in all

TABLE 1. Parameter Values for a Three-Layer Lithosphere

	Upper Crust	Lower Crust	Mantle Lithosphere	Asthenosphere
H_i, km	15	15	20 or 60	∞
n_i	10^3 or 3	3	3 or 10^3	3
ρ_i	2.8	2.8	3.2	3.15
$\bar{\eta}_i/\bar{\eta}_o$	1	10^{-2}	1	10^{-2}

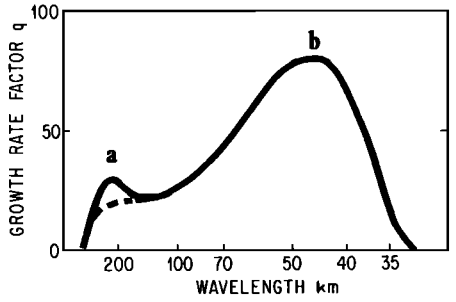

Fig. 5. Growth rate factor of stretching instabilities for a three-layer lithosphere consisting of a rheologically unstable upper crust (n_1=1000, thickness H_1=15 km), a soft lower crust (H_2=15 km) and a mantle lithosphere (H_3=20 or 60 km). This lithosphere lies upon an infinitely deep asthenosphere. All layers but the upper crust have a nonlinear rheology with n=3. The density contrasts $\delta\rho$ amount to 0.4 g/cm^3 at the Moho and -0.05 g/cm^3 at the lithosphere-asthenosphere boundary. The intensity of the gravitational stresses compared with the applied extensional stresses expressed by the ratio $\rho_1 g H_1/4\bar{\eta}_1\dot{\bar{\epsilon}}_{xx}$ amounts to 3. The dashed curve corresponds to the structure with a thicker mantle lithosphere (60 km). A gap exists on the short-wavelength side of this fundamental mode. The letters a and b refer to the submodes depicted in the next figure.

cases described in this section the density values, the viscosities, the crustal thicknesses H_1=H_2 and the power law coefficients of the soft crust and mantle layers n_2=n_4 remain unchanged. The thickness of the mantle lithosphere H_3 and the values of the power law coefficients for the strong layers n_1 and n_3 will be varied. As stated above, these three-layer models will be understandable on the basis of the physical concepts found in the last two sections with no essential addition. It is interesting, however,

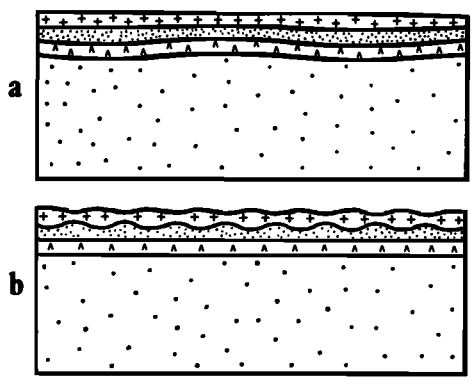

Fig. 6. Deformation pattern of a three-layer lithosphere with a rheologically unstable upper crustal layer. The two submodes depicted here correspond to the maxima a and b of the q curve of Figure 5. The finite deformation is not accessible by our physical analysis. Therefore only the relative amplitude and phase relationships at each interface are physically meaningful. Notice that the upper crust boudins at both wavelengths.

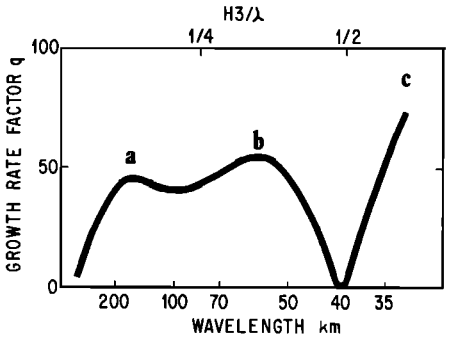

Fig. 7. Same plot as in Figure 5, but this time for a three-layer lithosphere where the rheologically unstable layer (n= 1000) is the mantle lithosphere of thickness H_3= 20 km. Other features are unchanged. The presence of a first overtone (c) is observed at short wavelengths (no gap).

to illustrate how the deformation of various layers can be coupled to each other.

Unstable Upper Crust

Let us first examine solutions where the upper crust alone is unstable (n_1=1000). Figure 5 depicts the computed growth rate factoras a function of the wavelength. The plot is restricted to wavelengths larger than 30 km as geophysical observations and regional tectonic trends are expected to exclude shorter wavelengths. The plot exhibits two distinct peaks. The largest peak (b) is centered around 55 km. It corresponds to the formation of pinch-and-swell instabilities within the crust with practically no deformation of the mantle lithosphere. This mode is illustrated in Figure 6b. It is very similar to the case of a

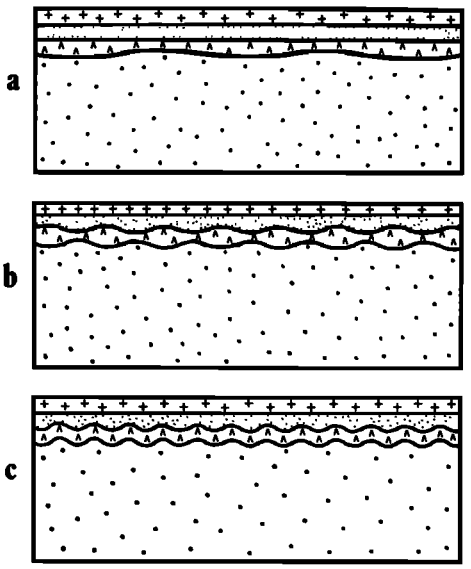

Fig. 8. Deformation pattern of the interfaces of a three-layer lithosphere corresponding to the three peaks a, b and c in the q curve of Figure 7. The rheologically unstable mantle lithosphere boudins in the first two sub-modes, and folds in the shorter-wavelength mode.

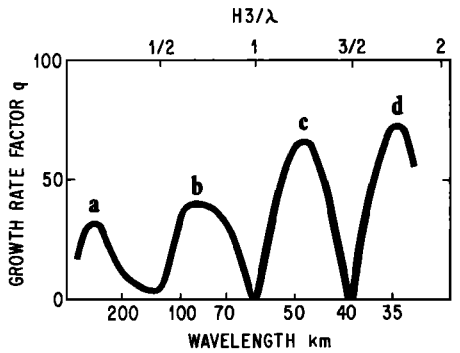

Fig. 9. Same q factor plot as in Figure 7 for a similar three-layer lithosphere. This time, however, the mantle layer is thicker (H_3=60 km and again n_3=1000). More overtones appear: a, b, c and d.

strong layer over a soft channel of equal thickness illustrated by the bottom curve in Figure 4. This comparison is also quite favorable as far as the value of the preferred wavelength λ is concerned. Again one finds that this induced short-wavelength topography is uncompensated and must be supported by internal stresses. In contrast to this, the long-wavelength mode pictured in Figure 6a has developed a crustal root which provides partial compensation. This Moho deflection is passively followed by the mantle lithospheric layer. The smaller peak (a) in the q curve of Figure 5 corresponds to this mode. It is centered around the wavelength of 220 km. One may interpret this larger wavelength in terms of an effective thickness of the whole lithospheric sandwich. This mode is less active when the mantle lithosphere is chosen to be 60 km thick rather than 20 km, as shown by the dashed curve in Figure 5. Shorter-wavelength overtones are not shown in Figure 5. A gap separates them from the plotted fundamental mode.

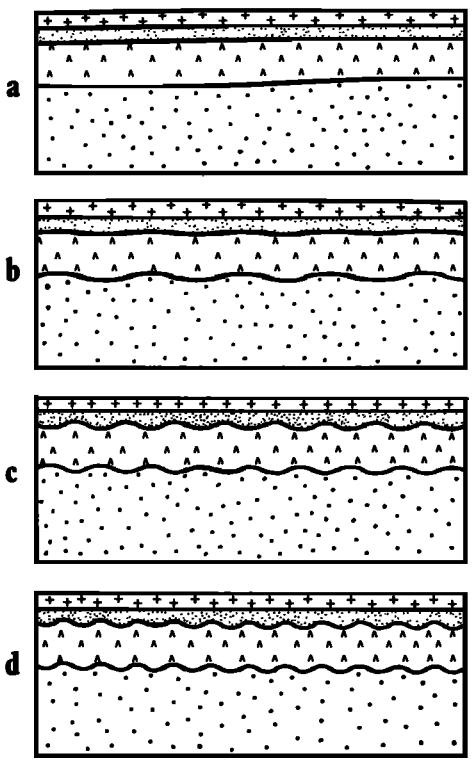

Fig. 10. Deformation patterns corresponding to the wavelengths of the different maxima a, b, c and d of the curve of Figure 9. As predicted, boudinage and buckling alternate.

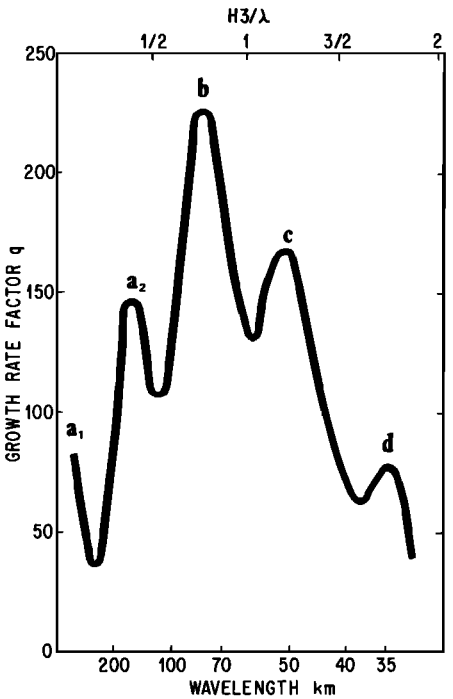

Fig. 11. Same q factor plot as in Figure 9 for a similar three-layer lithosphere (H_1=H_2=15 km, H_3=60 km). This time, however, both the upper crust and the mantle lithospheric layer are rheologically unstable (n_1=n_3=1000). This solution should be compared with Figure 7 and Figure 9 where only one of the two competent lithospheric layers is unstable.

Unstable Mantle Lithosphere

We next examine the response of a structure in the case where the mantle lithosphere alone is highly non-linear (n_3=1000). Two different thicknesses of the layer will be considered. Figures 7 and 8 depict the solutions for the case where H_3=20 km. As in Figure 1 we notice the existence of a fundamental mode in the range of wavelengths larger than 40 km, which is twice the width of the unstable layer. For shorter wavelengths, the plot of the growth rate factor q shows the beginning of the first overtone (c) where the unstable layer buckles rather than boudins as seen in Figure 8c. The two cartoons 8a and 8b correspond to the deformation pattern of each peak within the fundamental mode. Similarly to what we observed in the previous case, the inactive layer, now the upper crust, is either taking part passively in the deformation or remains unperturbed.

When the thickness of the unstable mantle lithospheric layer is increased to 60 km, several overtones appear in the range of wavelengths which is taken into consideration here (λ>30 km). This is shown in Figure 9. The vanishing q values

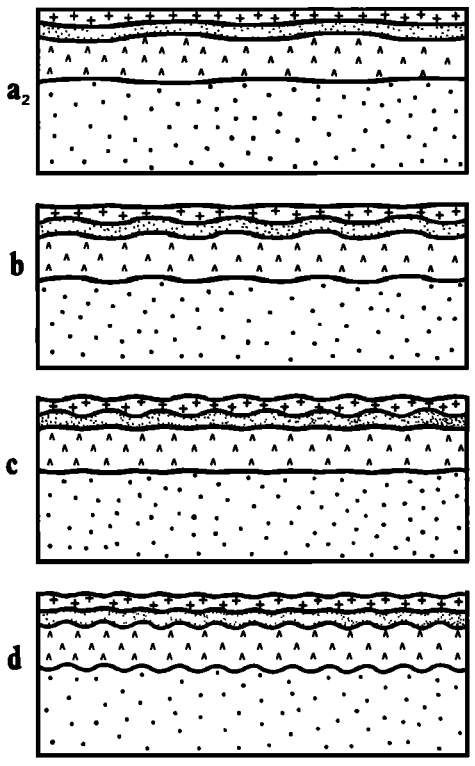

Fig. 12. Deformation patterns for a lithosphere structure with two rheologically active competent layers. Each cartoon a_2, b, c and d corresponds to a maximum in the q versus H_3/λ curve of Figure 11. These solutions should be compared with those of Figure 6 (unstable upper crust) and Figure 10 (unstable mantle lithosphere). Notice that the upper crust boudins at all wavelengths, whereas the mantle lithosphere alternates between boudinage and buckling.

between the various modes are found to correspond to wavelengths 120, 60, 40, 30,... km. This agrees with the prediction for the simple one-layer system of Figure 1. The fact that the first modes have a relatively small amplitude is to be attributed to the effect of gravity. The latter damps the long wavelengths more efficiently than the short ones. This can already be observed in Figure 2. One may also notice that the splitting of each mode into separate peaks is not resolved in the present case. However, a careful analysis of the deformation pattern of the fundamental mode reveals a change of concavity of the weak Moho deflection. This means that the pattern shown in Figure 10a, which corresponds to the fundamental mode, is in reality subdivided into two submodes. The next cartoons (Figures 10b-10d) illustrate the type of deformation corresponding to the maximum of the fundamental overtones. One notices alternate boudinage and buckling of the active layer. For the larger wavelengths the upper crust is passively involved in this deformation. It remains practically undeformed at the shorter wavelengths.

Lithosphere with Two Active Layers

Finally we illustrate a case where both the upper crust and the mantle lithosphere are unstable ($n_1=n_3=1000$, $H_3=60$ km). Figures 11 and 12 depict the variation of the growth rate factor q and the deformation pattern corresponding to its maxima. The q curve is equivalent to that of Figure 9 modulated by that of Figure 5. This means that the deformation is a composite of the crust-induced and mantle-induced instabilities. The comparison of Figures 11 and 9 shows that the extrema have kept their respective positions. For wavelengths larger than 120 km the two submodes (a_1 and a_2) which were hard to resolve in the previous case are now well separated. The four modes represented in Figure 12 show alternate buckling or boudinage instabilities of the 60-km-thick mantle layer. However, one should notice that all patterns fall within the fundamental boudinage mode of the active 15-km upper crust.

Conclusion

Suggestions that stretching instabilities could affect the crust as a whole, or even the lithosphere, prompted us to undertake a detailed physical study of such instabilities using a model structure. In its simplest form the latter consists of a competent layer imbedded in a weaker infinite matrix. Highly nonlinear rheologies like those where the rate of deformation $\dot{\epsilon}$ is proportional to the stress at a power $n \gg 1$ make the competent layer very unstable under extension or compression. Boudinage or folding instabilities can grow very rapidly around some preferred wavelength $\lambda = 4H$, but also at higher harmonics or overtones. We have shown that gravity tends to hamper or emphasize these instabilities, depending upon the sign of the density differences between layers. For instance we could quantify the shift in preferred wavelength, as well as the occurrence of forbidden gaps for certain ranges of wavelengths, caused by the stabilizing effect due to the density contrast at the earth's free surface. On the other hand, the density contrast at the lithosphere-asthenosphere boundary is destabilizing. It enhances the growth rate of instabilities when the lower lithosphere is actively involved. When possible, we have checked the agreement between analytical and computed solutions.

The idealized lithospheric structures investigated in the last section illustrate that several preferred wavelengths can be present simultaneously in a stratified structure undergoing stretching. It is therefore of primary interest to analyze geophysical data with these models in mind. In a situation like the Basin and Range province in western North America, the question is now to find out if the topography and Bouguer anomaly patterns contain dominant wavelengths and if so, what are their respective azimuthal orientations and with what tectonic phase might they be connected? In a future study we plan to present some answers to such questions. In regions where the data are more sparse (e.g., Tibet or northeast China), one may also find it relevant to plan deep structural studies by seismic and gravity methods to look for possible correlations between surface features and Moho and deeper configurations.

Of course the earth's lithosphere may be even more nonlinear mechanically than our extreme stratified model structures. It may also contain

inherited discontinuities, such as deeply penetrating faults. However, we consider the present investigation as a necessary step to clarify the basic mechanisms that yield some of the observed regularities in the length range 20 to 200 km in tectonic provinces such as those mentioned above.

Appendix A

A general solution with sinusoidal dependence along the horizontal axis can be found for the perturbing flow:

$$w=(a_1f_1(z)+a_2f_2(z)+a_3f_3(z)+a_4f_4(z))\cos kx \quad (A1a)$$

$$u=((-\alpha a_1-\beta a_2)f_1(z)+(-\alpha a_2+\beta a_1)f_2(z)+(\alpha a_3-\beta a_4)f_3(z)+(-\alpha a_4-\beta a_3)f_4(z))\cos kx \quad (A1b)$$

$$zz=-2\eta\alpha k((a_1f_1(z)+a_2f_2(z)-a_3f_3(z)-a_4f_4(z))\cos kx \quad (A1c)$$

$$xz=-2\eta\alpha k((-\alpha a_1-\beta a_2)f_1(z)+(-\alpha a_2+\beta a_1)f_2(z)-(\alpha a_3-\beta a_4)f_3(z)-(-\alpha a_4-\beta a_3)f_4(z))\sin kx \quad (A1d)$$

where

$f_1(z)=\cos\beta kz \quad \exp\alpha kz$
$f_2(z)=\sin\beta kz \quad \exp\alpha kz$
$f_3(z)=\cos\beta kz \quad \exp-\alpha kz$
$f_4(z)=\sin\beta kz \quad \exp-\alpha kz$

As most other authors, we introduced the parameters α and β, which are simple functions of the power law coefficient:

$$\alpha=\sqrt{\frac{1}{n}} \qquad \beta=\sqrt{\frac{n-1}{n}} \quad (A2)$$

Appendix B

The equations (3) which express the difference in stresses between two horizontal layers on both sides of a deflected boundary can be written in the form

$$\tilde{\sigma}_{zz}^{b}=\tilde{\sigma}_{zz}^{a}+\delta\rho gh$$
$$\tilde{\sigma}_{xz}^{b}=\tilde{\sigma}_{xz}^{a}+4(\bar{\eta}_1-\bar{\eta}_2)\dot{\bar{\epsilon}}_{xx}kh \quad (B1)$$

In the half-space referred by the index a, the general solutions for the velocity and the stresses must vanish at infinity. By inspection of (A1), this leads to the simple relationships

$$\tilde{\sigma}_{zz}^{a}=-2\bar{\eta}_2\alpha_2k\tilde{w}$$
$$\tilde{\sigma}_{xz}^{a}=-2\bar{\eta}_2\alpha_2k\tilde{u} \quad (B2)$$

These equations are well known for glacial post-rebound problems in the case of Newtonian rheologies where $\alpha_2=1$.

The vertical velocity $\tilde{w}$ at the interface is identical to $\dot{h}-\dot{\bar{\epsilon}}_{xx}h$. From the continuity equation, one can derive the vertically averaged horizontal velocity $\langle\tilde{u}\rangle$:

$$k\langle\tilde{u}\rangle+2\frac{\tilde{w}}{H_1}=0 \quad (B3)$$

Finally, an integration by parts ($-H_1/2<z<H_1/2$) yields $\tilde{u}$ as a function of $\langle\tilde{u}\rangle$ and h. In this calculation, only the terms of order larger than kH_1 are kept.

$$\langle\tilde{u}\rangle=\frac{1}{H_1}\int\tilde{u}\,dz=\tilde{u}-\frac{1}{H_1}\int\frac{\partial\tilde{u}}{\partial z}z\,dz\simeq\tilde{u}-\frac{1}{H_1}\int k\tilde{w}z\,dz$$
$$\langle\tilde{u}\rangle\simeq\tilde{u}-\frac{k\tilde{w}}{H_1}\int z^2\,dz\simeq\tilde{u}-\frac{1}{6}kH_1\tilde{w} \quad (B4)$$

The combination of (B1) to (B4) yields the expressions of the stresses at the deflected boundary versus h and $\dot{h}$.

$$\tilde{\sigma}_{zz}^{b}=\delta\rho gh-2\frac{\bar{\eta}_2}{\sqrt{n_2}}k(\dot{h}-\dot{\bar{\epsilon}}_{xx}h)$$
$$\tilde{\sigma}_{xz}^{b}=4(\bar{\eta}_1-\bar{\eta}_2)\dot{\bar{\epsilon}}_{xx}kh+\frac{\bar{\eta}_2}{\sqrt{n_2}}\frac{1}{H_1}(\dot{h}-\dot{\bar{\epsilon}}_{xx}h)(1-\frac{1}{12}k^2H_1^2) \quad (B5)$$

References

Armijo R., P. Tapponier, J. L. Mercier, and Han T., A field study of Pleistocene rifts in Tibet, Eos Trans. AGU, 63, 1093, 1982.

Biot, M. A., Theory of folding of stratified viscoelastic media and its implications in tectonics and orogenesis, Bull. Geol. Soc. Am., 72, 1595-1620, 1961.

Biot, M. A., H. Odé, W. L. Roever, Experimental verification of the theory of folding of stratified viscoelastic media., Bull. Geol. Soc. Am., 72, 1621-1632, 1961.

Fleitout, L., and D. A. Yuen, Steady-state, secondary convection beneath a lithospheric plate with pressure and temperature dependent viscosity, J. Geophys. Res., 89, 9227-9244, 1984.

Fletcher, R. C., Wavelength selection in the folding of a single layer with power-law rheology, Am. J. Sci., 274, 1029-1043, 1974.

Fletcher, R. C. and B. Hallet, Unstable extension of the lithosphere: A mechanical model for Basin and Range structure, J. Geophys. Res., 88, 7457-7466, 1983.

Froidevaux, C., Basin and Range large scale tectonics: Constraints from gravity and reflection seismology, J. Geophys. Res., 91, 3625-3632, 1986.

Froidevaux, C., and Y. Ricard, Tectonics evolution of high plateaus, Tectonophysics in press, 1986.

Johnson, A. M., Styles of folding, Elsevier Scientific, New York, 1977.

Humphreys, E., R. W. Clayton and B. Hager, A tomographic image of mantle structure beneath Southern California, Geophys. Res. Lett., 11(7), 625-628, 1984.

Ma X., Liu G., and Su J., The structure and dynamics of the continental lithosphere in north-northeast China, Ann. Geophys., 6, 614-620, 1984.

Marillier, F., and S. Mueller, Structure of the upper mantle in the northeastern Atlantic close to the Azores-Gibraltar ridge from surface wave and body wave observations, Tectonophysics, 90, 195-213, 1982.

Montagner, J. P., Regional three-dimensional structures using long-period surface waves, Ann. Geophys., in press, 1986.

Neurath, C., and R. B. Smith, The effect of material properties on growth rates of folding and boudinage: Experiments with wax models, J. Struct. Geol., 4(2), 215-229, 1982.

Ramberg, H., Natural and experimental boudinage and pinch-and-swell structures, J. Geol., 63, 512-526, 1955.

Ramberg, H., Fluid dynamics of viscous buckling applicable to the folding of layered rocks : Am. Assoc. Pet. Geol. Bull., 47, 484-505, 1963.

Ricard, Y. , doctoral thesis, Univ. de Paris-Sud, Orsay, France, Dynamique interne de la terre et observations gravimetriques, 1986.

Smith, R. B., Formation of folds, boudinage and mullions in non Newtonian materials, Geol. Soc. Am. Bull., 88, 312-320, 1977.

Smith, R. B., The folding of a strongly non Newtonian layer., Am. J. Sci., 279, 272-287, 1979.

Zuber, M. T., E. M. Parmentier and R. C. Fletcher, Extension of continental lithosphere: a model for two scales of Basin and Range deformation, J. Geophys. Res., 91, 4826-4838, 1986.

Y. Ricard and C. Froidevaux, Laboratoire de Géodynamique, Université de Paris-Sud, Bâtiment 510, 91405 Orsay, France.

(Received September 4, 1985;
revised January 7, 1986;
accepted February 10, 1986.)